Measurement 257 (2026) 118975

Contents lists available at ScienceDirect

Measurement

journal homepage: www.elsevier.com/locate/measurement

Fast and accurate estimation of real-valued damped sinusoid amplitude and phase

Daniel Belega [a,*], Dario Petri [b]

[a] Department of Measurements and Optical Electronics, Politehnica University Timişoara, Bv. V. Pârvan, Nr. 2, 300223 Timişoara, Romania
[b] Department of Industrial Engineering, University of Trento, Via Sommarive 9, Povo, Trento 38123, Italy

ARTICLE INFO

Keywords:
Interpolated discrete Fourier transform algorithm
Parameter estimation
Real-valued damped sinusoids
Statistical analysis
Windowing

ABSTRACT

This paper proposes fast amplitude and phase estimators for real-valued damped sinusoid based on the classical Interpolated Discrete Fourier Transform (IpDFT) algorithm and the Maximum Sidelobe Decay (MSD) windows. To this aim, at first analytical expressions for the contribution of the fundamental image component on the IpDFT estimates are derived. Then, exploiting the derived expressions new amplitude and phase estimators are proposed. The achievable accuracy is investigated by using both simulation and experimental results related to real-valued noisy or noisy and distorted damped sinusoids. Moreover, the performance of the proposed algorithm, and three other state-of-the-art algorithms are compared to each other considering both simulated and experimental data.

1. Introduction

Accurate real-time estimation of real-valued damped sinusoids parameters is often required in many application domains such as nuclear magnetic resonance [1,2], atomic magnetometers [3–5], optics [6,7], power systems [8,9], and quartz crystal microbalances with dissipation monitoring [10]. To this aim both time-domain and frequency-domain algorithms have been proposed. Time-domain estimators, also known as parametric algorithms, provide almost optimal accuracy, but they are sensitive to the adopted signal model and the required computational burden is relevant since matrix operations must be performed. Two state-of-the-art widely employed time-domain procedures are the Prony method [11–13] and the Matrix Pencil (MP) algorithm [11,14–16].

Conversely, frequency-domain estimators, also known as nonparametric algorithms, exploit only selected Discrete Time Fourier Transform (DTFT) samples of the analyzed signal. They are robust to the adopted signal model and require a small computational burden, but the estimation accuracy is often worse than the one returned by time-domain algorithms. Among such estimators the Interpolated Discrete Transform (IpDFT) based algorithms are widely used in practice since they compensate for the picket-fence effect due to the discrete spectrum granularity [17] ensuring a low computational effort. IpDFT algorithms based on two [18–24] or more interpolation [25–30] points have been proposed in the literature. The classical IpDFT algorithm estimates the fractional bin frequency and the decay rate by interpolating the two highest DFT spectrum samples of the analyzed signals [11,18–23]. Other IpDFT algorithms exploit more interpolation points to compensate for the detrimental contribution of the fundamental image component on the estimated parameters. Before performing the time–frequency transformation, the signal can be weighted by a suitable window in order to reduce the spectral leakage due to the finite observation length. The Maximum Sidelobe Decay (MSD) windows are often used since they exhibit very good sidelobe decay rate – equal to $6(2H-1)$ dB/octave, for the H-term window – so ensuring a high rejection of the contribution of any disturbing signal tones to the estimated parameters [31]. In addition, the parameters of interest can be estimated by using very simple analytical expressions [23]. In particular, the two-term MSD window ($H=2$), also known as the Hann window, is widely used since it ensures both a relatively low Equivalent Noise BandWidth (*ENBW*) and effective rejection of disturbing tones due to a sidelobe decay equal to 18 dB/octave [21,23,26,27].

Many time-domain algorithms, such as the Prony method and the MP algorithm, firstly estimate the signal frequency and decay rate [12,15]. Exploiting the knowledge on these two parameters, the signal amplitude and phase are then determined by means of a linear least square approach. IpDTFT algorithms follow a similar approach since the signal frequency and decay rate are firstly estimated [10,11,17–30]. Then, the signal amplitude and phase are often extracted from the DFT sample

* Corresponding author.
E-mail addresses: daniel.belega@upt.ro (D. Belega), dario.petri@unitn.it (D. Petri).

https://doi.org/10.1016/j.measurement.2025.118975
Received 10 April 2025; Received in revised form 3 September 2025; Accepted 10 September 2025
Available online 13 September 2025

corresponding to the fundamental frequency [23]. Unfortunately, the estimated parameters can be heavily affected by the contribution of the fundamental image component, especially when a small number of signal cycles is analyzed.

Most of the IpDTFT algorithms are limited to frequency and decay rate estimation, while only few of them estimate all the parameters of damped sinusoid. In [11] and [25] three-point IpDFT algorithms for the estimation of the parameters of a multifrequency real-valued noise damped sinusoid have been proposed. Since they are based on the rectangular window, the contribution of the fundamental image component and other disturbing tones on the estimated parameters can be relevant, so that computationally expensive iterations are needed to obtain accurate results. In [23] analytical expressions for the contribution of the fundamental image component to the signal frequency and decay rate estimates returned by the classical IpDFT algorithm based on an MSD window have been derived. However, to the authors' best knowledge, similar expressions for the IpDFT amplitude and phase estimates have not been derived yet. This paper is aimed at deriving them and at their exploitation a new IpDFT damped sinusoid amplitude and phase estimator, named in the following the c-IpDFTds algorithm. As compared with the procedures proposed in [11] and [25], the c-IpDFTds algorithm reduces the interference from disturbing tones by weighting the acquired signal samples with an MSD window, so avoiding the need for an iterative procedure.

Leveraging on both simulation and experimental results, the accuracy of the proposed c-IpDFTds algorithm is investigated and compared with the best accuracy provided by the classical IpDFT algorithm, the Bertocco-Yoshida order 1 with leakage correction (BY1-LC) algorithm [11,27], the Prony algorithm [11–13], and the MP algorithm [11,14–16]. The processing times required by the analyzed algorithms are also compared to each other.

The remaining of the paper is organized as follows. In Section 2 the aforementioned analytical expressions are derived. The proposed c-IpDFTds algorithm is then presented in Section 3. Sections 4 and 5 investigate the accuracies of the derived expressions and the c-IpDFTds algorithm, respectively. Section 6 deals with the algorithm processing times. Section 7 provides some conclusions.

2. Contribution of the fundamental image component to the IpDFT amplitude and phase estimators

The acquired real-valued damped sinusoid is modelled as:

$$x(m) = Ae^{-\frac{2\pi}{M}\alpha m}\cos\left(2\pi\frac{\nu}{M}m+\phi\right), m = 0,1,\cdots,M-1 \tag{1}$$

where A, ν, ϕ, and α are the signal amplitude, the normalized frequency, the initial phase, and the normalized decay rate, respectively. M is the number of samples or the acquisition length. The normalized frequency ν represents the number of analyzed signal cycles and it can be expressed as:

$$\nu = l+\delta, \tag{2}$$

where l is an integer and $-0.5 \le \delta < 0.5$. The fractional frequency δ is null when coherent sampling occurs. The normalized decay rate α represents the ratio between twice π the signal time constant and the observation interval duration. That variable has been selected to exploit the similarity with the normalized frequency ν.

The contribution of the fundamental image component on the estimated parameters can be reduced by weighting signal (1) with a suitable window $w(m)$, so obtaining the signal $x_w(m) = x(m)\cdot w(m)$. In the following the MSD windows are employed due to their previously mentioned properties. The generic H-term MSD window is defined as:

$$w(m) = \sum_{h=0}^{H-1}(-1)^h a_h \cos\left(\frac{2\pi hm}{M}\right), m = 0,1,\cdots,M-1 \tag{3}$$

where $a_0 = \frac{C_{2H-2}^{H-1}}{2^{2H-2}}$, and $a_h = \frac{C_{2H-2}^{H-1-h}}{2^{2H-3}}$, $h = 1, 2, \cdots, H-1$ with $C_n^q = \frac{n!}{(n-q)!\bullet q!}$ [32]. In particular, for the two-term MSD window ($H = 2$) the coefficients are: $a_0 = 0.5$ and $a_1 = 0.5$.

The DTFT of the windowed signal $x_w(m)$ can be expressed as:

$$X_w(\lambda) = X_{fw}(\lambda) + X_{iw}(\lambda), \lambda \in [0, M) \tag{4}$$

where $\widetilde{X}_{fw}(\lambda)$ and $\widetilde{X}_{iw}(\lambda)$ are the DTFT of the fundamental and the spectral image components, respectively. They can be expressed as follows [23]:

$$X_{fw}(\lambda) \cong A\Psi(\alpha+\mathrm{j}(\lambda-\nu))e^{\mathrm{j}\phi} \tag{5a}$$

and

$$X_{iw}(\lambda) \cong A\Psi(\alpha+\mathrm{j}(\lambda+\nu))e^{-\mathrm{j}\phi}, \tag{5b}$$

where

$$\Psi(z) \triangleq \frac{(2H-2)!}{2^{2H}}\frac{M}{\pi}\frac{1-e^{-2\pi z}}{z\prod_{h=1}^{H-1}(z^2+h^2)}, \tag{6}$$

in which z is a complex-valued variable.

The fractional frequency and normalized decay rate estimators provided by the IpDFT algorithm based on the H-term MSD window are given by [23]:

$$\widehat{\delta} = sRe\left\{\frac{H\rho+H-1}{\rho-1}\right\}, \tag{7}$$

and

$$\widehat{\alpha} = sIm\left\{\frac{H\rho+H-1}{\rho-1}\right\}, \tag{8}$$

where $\rho = \frac{X_w(l+s)}{X_w(l)}$, $s = sgn(|X_w(l+1)|-|X_w(l-1)|)$, in which $sgn(\bullet)$ is the sign function. Re{•} and Im{•} are the real and the imaginary operators.

If the normalized decay rate is not too high and enough signal cycles are observed (in the following these constraints are quantified by simulation results), the contribution of the fundamental image component $X_{iw}(\lambda)$ to (4) can be neglected. Thus, the IpDFT amplitude and phase estimators can be easily derived from (5a) as:

$$\widehat{A} = \left|\frac{X_w(l)}{\Psi(\widehat{\alpha}-\mathrm{j}\widehat{\delta})}\right|, \tag{9}$$

and

$$\widehat{\phi} = arg\left\{\frac{X_w(l)}{\Psi(\widehat{\alpha}-\mathrm{j}\widehat{\delta})}\right\}. \tag{10}$$

The following Propositions hold (see the Appendix for the proofs).

Proposition 1. (*The relative contribution of the fundamental image component to IpDFT amplitude estimate (9) is:*)

$$\varepsilon_A \triangleq \frac{\Delta A}{A} = \frac{\widehat{A}-A}{A} \cong \frac{|\Psi(\alpha-\mathrm{j}\delta)|}{|\Psi(\widehat{\alpha}-\mathrm{j}\widehat{\delta})|}\left[1+\frac{|\Psi(\alpha+\mathrm{j}(2l+\delta))|}{|\Psi(\alpha-\mathrm{j}\delta)|}\bullet\cos(2\phi+\gamma_1-\gamma_2)\right]-1, \tag{11}$$

where γ_1 and γ_2 are the phases of $\Psi(\alpha - j\delta)$ and $\Psi(\alpha + j(2l + \delta))$, respectively.

Proposition 2. (*The contribution of the fundamental image component to IpDFT phase estimate (10) is:*)

$$\Delta\phi \triangleq \widehat{\phi}-\phi \cong \gamma_1-\widehat{\gamma}_1-\frac{|\Psi(\alpha+\mathrm{j}(2l+\delta))|}{|\Psi(\alpha-\mathrm{j}\delta)|}\bullet\sin(2\phi+\gamma_1-\gamma_2), \tag{12}$$

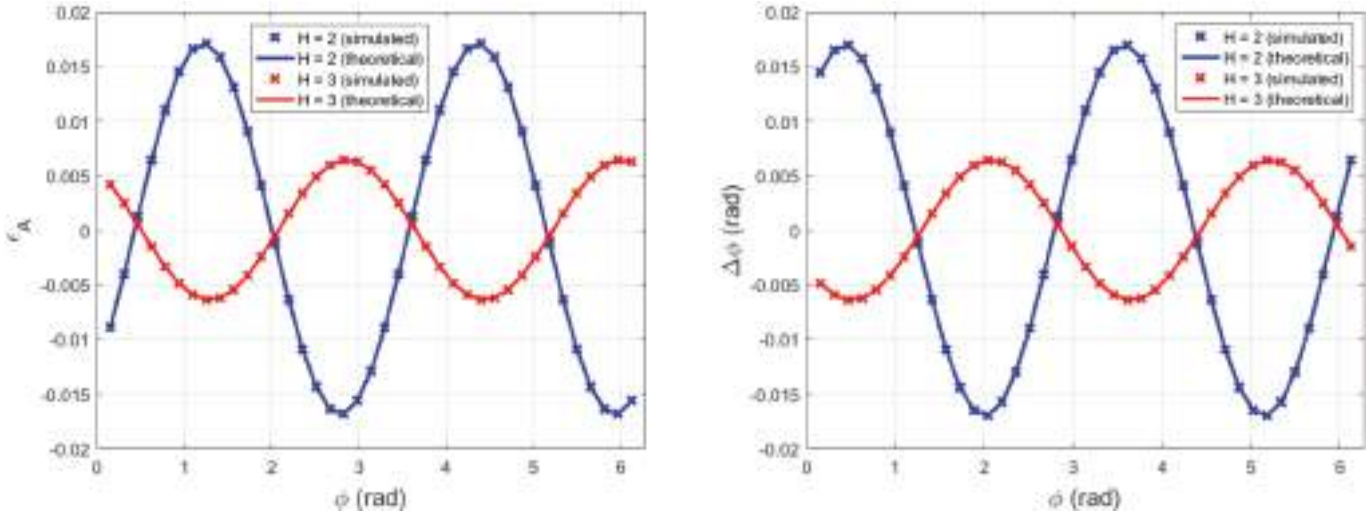

Fig. 1. Pure real-valued damped sinusoids: values of ε_A (a) and $\Delta\phi$ (b) returned by (11), (12) and simulations versus the signal phase ϕ. $\alpha = 0.2$, $\nu = 2.3$ cycles. Two-term MSD ($H = 2$) window and three-term MSD ($H = 3$) window. For each value of ν, 10,000 runs of $M = 128$ samples are considered.

where $\widehat{\gamma}_1$ is the phase of $\Psi(\widehat{\alpha} - \mathrm{j}\widehat{\delta})$.

3. The IpDFT compensated algorithm

When the H-term MSD window is employed, the contribution of the fundamental image component to the IpDFT fractional frequency and decay rate estimators are [23]:

$$\Delta\delta \triangleq \widehat{\delta} - \delta \cong Re\{\vartheta(\alpha, l, \delta, \phi, H)\}, \tag{13}$$

and

$$\Delta\alpha \triangleq \widehat{\alpha} - \alpha \cong Im\{\vartheta(\alpha, l, \delta, \phi, H)\}, \tag{14}$$

where

$$\vartheta(\alpha, l, \delta, \phi, H) \triangleq -2\nu \frac{\alpha - \mathrm{j}(\delta - sH)}{\alpha + \mathrm{j}(2l + \delta + sH)} \bullet \frac{\Psi(\alpha + \mathrm{j}(2l + \delta))}{\Psi(\alpha - \mathrm{j}\delta)} \bullet e^{-2\mathrm{j}\phi}$$
$$= -2\nu \frac{\alpha - \mathrm{j}(\delta - sH)}{\alpha + \mathrm{j}(2l + \delta + sH)} \bullet \frac{\alpha - \mathrm{j}\delta}{\alpha + \mathrm{j}(2l + \delta)}$$
$$\times \frac{1 - e^{-2\pi(\alpha + \mathrm{j}\delta)}}{1 - e^{-2\pi(\alpha - \mathrm{j}\delta)}} \frac{\prod_{h=1}^{H-1}\left[(\alpha - \mathrm{j}\delta)^2 + h^2\right]}{\prod_{h=1}^{H-1}\left[(\alpha + \mathrm{j}(2l + \delta))^2 + h^2\right]} \bullet e^{-2\mathrm{j}\phi}. \tag{15}$$

Expressions (11)-(15) enable the definition of the following c-IpDFTds algorithm, in which the classical two-point IpDFT algorithm (steps 1–5) is followed by the signal amplitude and phase compensation (steps 6–10).

% classical IpDFT algorithm

step 1: *acquire M samples of the real-valued damped sinusoid x(m);*

step 2: *compute the DFT $X_w(k)$ of the weighted signal $x_w(m) = x(m) \cdot w(m)$;*

step 3: *determine the integer part l of the normalized frequency as the location of the DFT spectrum peak;*

step 4: *apply (7) and (8) to obtain the initial estimates $\widehat{\delta}$ and $\widehat{\alpha}$ of the fractional frequency and normalized decay rate, respectively;*

step 5: *apply (9) and (10) to obtain the initial estimates $\widehat{A}$ and $\widehat{\phi}$ of the signal amplitude and phase, respectively;*

% amplitude and phase compensation

step 6: *apply (6) with $z = \widehat{\alpha} - \mathrm{j}\widehat{\delta}$ and evaluate the phase $\widehat{\gamma}_1$ of $\psi(\widehat{\alpha} - \mathrm{j}\widehat{\delta})$;*

step 7: *apply (15) and evaluate $\vartheta(\widehat{\alpha}, l, \widehat{\delta}, \widehat{\phi}, H)$;*

step 8: *apply (13) and (14) to compensate the contributions of the image component to the results of step 4: $\widehat{\delta}_c \cong \widehat{\delta} - Re\{\vartheta(\widehat{\alpha}, l, \widehat{\delta}, \widehat{\phi}, H)\}$ and $\widehat{\alpha}_c \cong \widehat{\alpha} - Im\{\vartheta(\widehat{\alpha}, l, \widehat{\delta}, \widehat{\phi}, H)\}$;*

step 9: *apply (6) to evaluate the phases γ_{1c} and γ_{2c} of $\psi(\widehat{\alpha}_c - \mathrm{j}\widehat{\delta}_c)$ and $\psi(\widehat{\alpha}_c + \mathrm{j}(2l + \widehat{\delta}_c))$;*

% return the c-IpDFTds amplitude and phase estimates

step 10: *using $\widehat{\delta}_c$, $\widehat{\alpha}_c$, γ_{1c}, γ_{2c}, and $\widehat{\phi}$, apply (11) and (12) to compensate the contributions, ε_A and $\Delta\phi$, of the image component to the results of step 5, so obtaining the final amplitude and phase estimates: $\widehat{A}_c = \widehat{A}(1 - \varepsilon_A)$ and $\widehat{\phi}_c = \widehat{\phi} - \Delta\phi$.*

4. Accuracy of the expressions for the contribution of the fundamental image component

The accuracies of expressions (11) and (12) are verified in the following by means of computer simulations. The amplitude of the real-valued damped sinusoids is $A = 1$p.u. and the acquisition length is $M = 128$ samples.

Fig. 1 shows the quantities ε_A (Fig. 1(a)) and $\Delta\phi$ (Fig. 1(b)) returned by (11), (12), and by simulations as a function of the signal phase ϕ, which varies in the range [0, 2π) rad with a step of π/20 rad. $\nu = 2.3$ cycles of a pure real-valued damped sinusoid with normalized decay rate $\alpha = 0.2$ are analyzed. The two-term MSD (or the Hann) ($H = 2$) window and the three-term MSD ($H = 3$) window are used.

As we can see, there exists a very good agreement between the theoretical and the simulation results. It is worth observing that the image component contribution to both obtained estimates is lower for the three-term MSD window. Indeed, further simulations performed with different number of observed cycles showed that the three-term MSD window ensures more accurate results as long as at least about 1.5 cycles are observed independently of the number of processed samples in the range $32 \leq M \leq 4096$.

5. Accuracy of the proposed algorithm

In the following, both computer simulations and experimental results are employed to compare the accuracies of the proposed c-IpDFTds, the classical IpDFT [23] algorithms, the BY1-LC algorithm [11,27], the

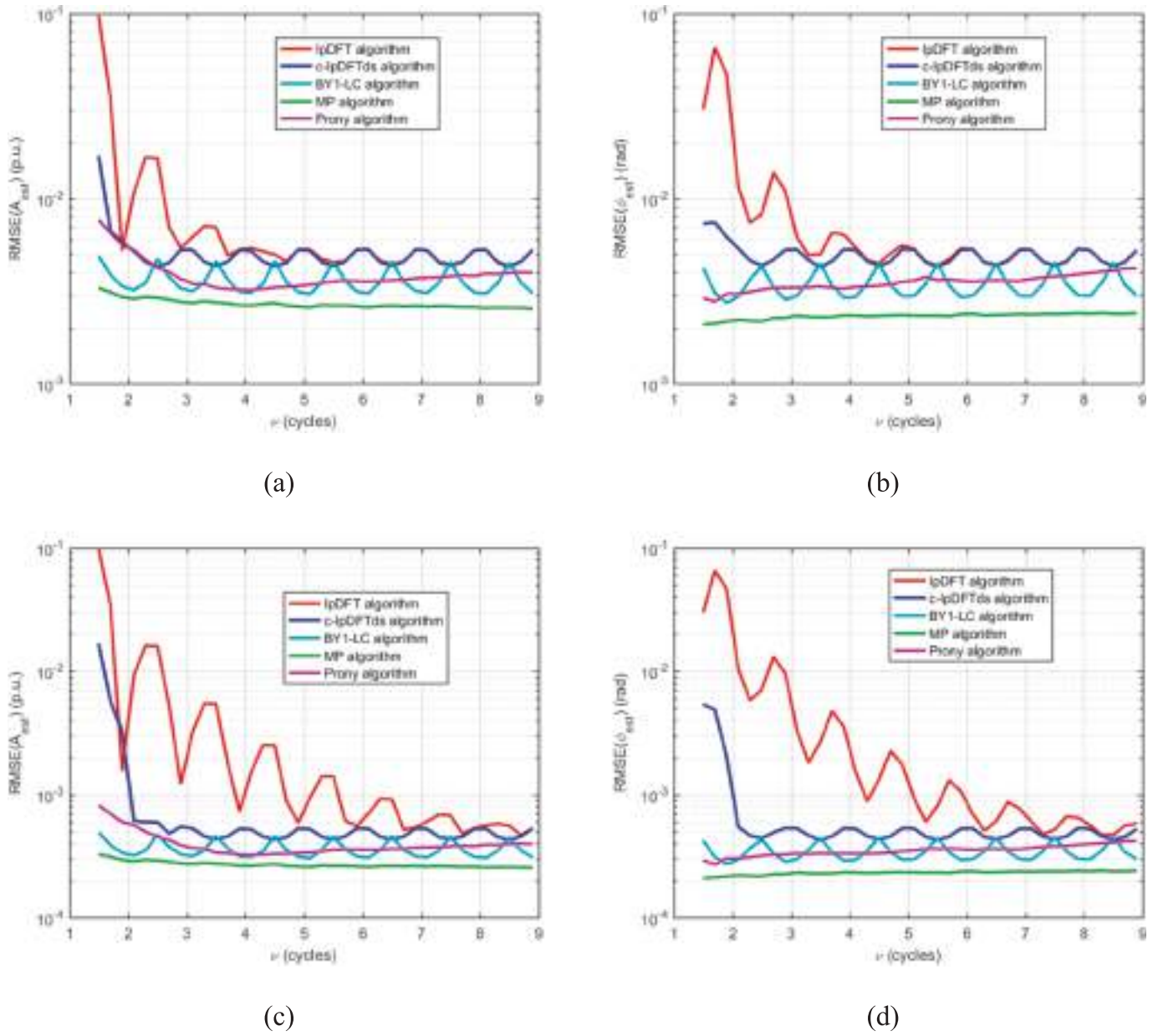

Fig. 2. Real-valued noisy damped sinusoids: *RMSE*s of the amplitude (a), (c) and the phase (b), (d) estimates returned by the IpDFT, the c-IpDFTds, the BY1-LC, the MP, and the Prony algorithms versus the normalized frequency ν. $SNR = 40$ dB (a), (b) or 60 dB (c), (d), $\alpha = 0.2$. The two-term MSD ($H = 2$) window is adopted in the IpDFT and the c-IpDFTds algorithms. 10 iteratios are used in the BY1-LC algorithm, and the number of signal components is assumed known in the MP and the Prony algorithms. For each value of ν, 10,000 runs of $M = 128$ samples are considered.

Prony [11,12], and the MP [11,14] algorithms. In the performed analysis 10 iterations are performed for the BY1-LC algorithm [11]. Regarding the considered time-domain algorithms, it is well established that their accuracies are highly sensitive to the choice of the model order [12,15]. Moreover, simulation results indicate that the optimal model order is strongly influenced by the number of signal components, which is typically unknown in engineering applications. Nevertheless, since a detailed investigation of the effect of the model order on the Prony and the MP algorithm accuracies is beyond the scope of this paper, in the following it is assumed that both these time-domain based algorithms have access to the true number of signal components, thereby operating at their best accuracy. This assumption does not hold when processing experimental data, where the number of signal components is unknown. In that case, the model order for the MP algorithm is determined by applying the procedure proposed in [15].

5.1. Computer simulations

Monte Carlo simulations are performed considering both real-valued noisy or noisy and harmonically distorted damped sinusoids. The sinusoid amplitude is $A = 1$p.u and the acquisition length is $M = 128$ samples. When real-valued damped sinusoids are analyzed, extensive simulations suggested that almost optimal accuracy can be obtained when the Prony model order (i.e., the number of polynomial coefficients) is $P = 16$ or $P = 11$ when less than about 5 cycles or more than about 6 cycles are observed. As for the MP algorithm, the model order K is selected equal to twice the number of signal components (which is assumed to be known), as suggested in the literature [14]. In addition, the pencil parameter is chosen equal to $M/2$ in order to approach the Cramér-Rao Lower Bound (CRLB) [16]. The phase of the fundamental component is equal to $\pi/3$ rad, but further simulations showed that the results reported in the following hold regardless of the signal phase. For

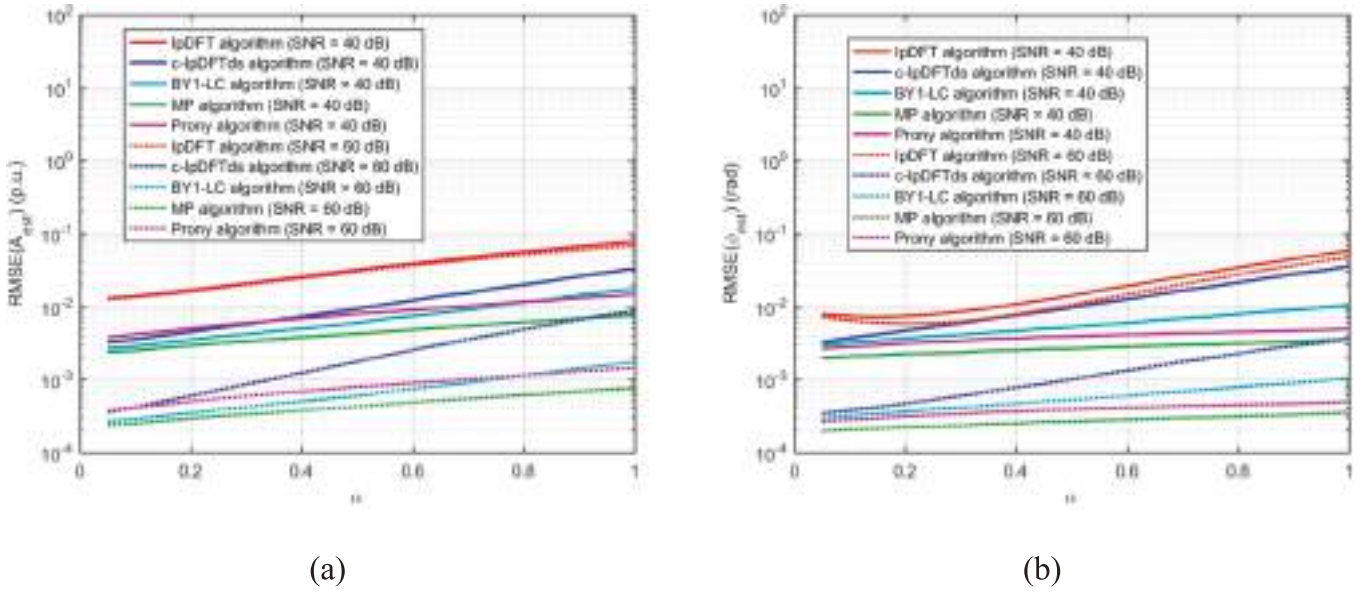

Fig. 3. Real-valued noisy damped sinusoids: *RMSE*s of the amplitude (a), and the phase (b) estimates returned by the IpDFT, the c-IpDFTds, the BY1-LC, the MP, and the Prony algorithms versus the decay rate α. $\nu = 2.3$ cycles, $SNR = 40$ dB or $SNR = 60$ dB. The two-term MSD ($H = 2$) window is adopted in the IpDFT and the c-IpDFTds algorithms. 10 iteratios are used in the BY1-LC algorithm, and the number of signal components is assumed known in the MP and the Prony algorithms. For each value of α, 10,000 runs of $M = 128$ samples each are considered.

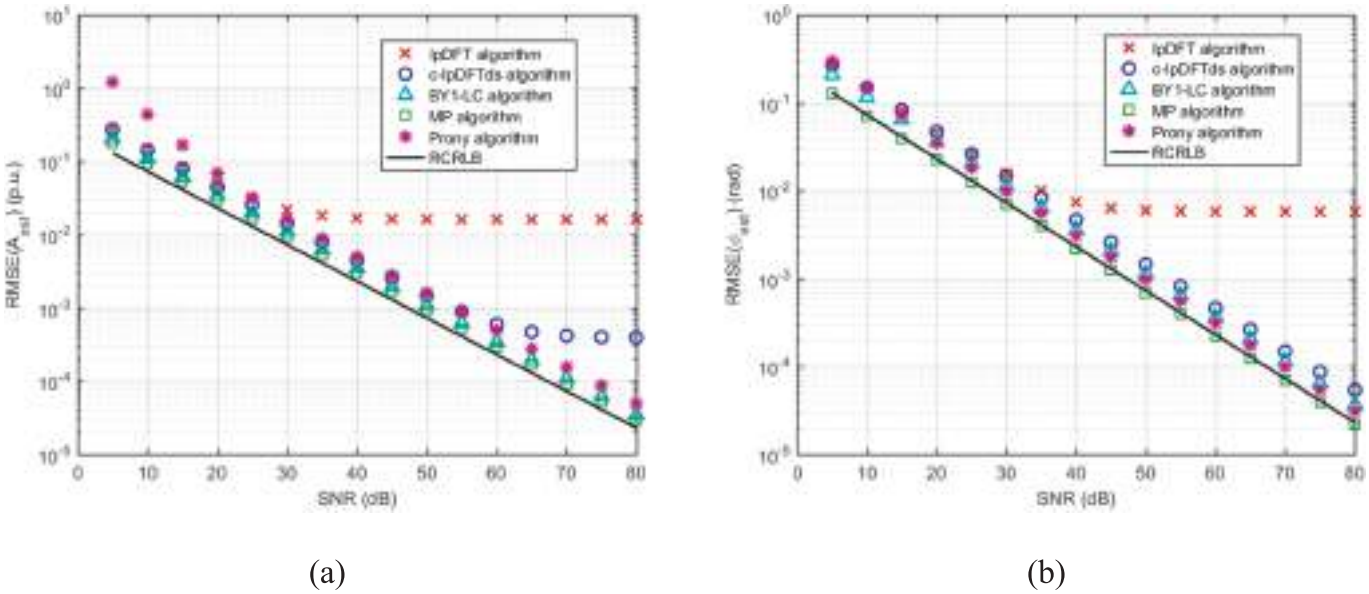

Fig. 4. Real-valued noisy damped sinusoids: *RMSE*s of the amplitude (a), and the phase (b) estimates returned by the IpDFT, the c-IpDFTds, the BY1-LC, the MP, and the Prony algorithms versus *SNR*. $\nu = 2.3$ cycles and $\alpha = 0.2$. The two-term MSD ($H = 2$) window is adopted in the IpDFT and the c-IpDFTds algorithms. 10 iteratios are used in the BY1-LC algorithm, and the number of signal components is assumed known in the MP and the Prony algorithms. For each value of *SNR*, 10,000 runs of $M = 128$ samples each are considered.

each value of the variable parameter 10,000 runs are performed and the Root Mean Square Errors (*RMSE*s) of the returned amplitude and phase estimates are computed. For the IpDFT and the c-IpDFTds algorithms, only the results related to the two-term MSD ($H = 2$) window are discussed since the same behavior is obtained when a higher order window is adopted even if the *RMSE* values may increase with the window order.

Fig. 2 shows the *RMSE*s of the amplitude and the phase estimators as a function of the normalized frequency ν, which varies with a step of 0.2 cycles. The normalized decay rate is $\alpha = 0.2$ and the *SNR* is equal to 40 dB (Fig. 2(a) and (b)) or 60 dB (Fig. 2(c) and (d)).

As expected, the proposed c-IpDFTds algorithm outperforms the classical IpDFT algorithm, especially when the contribution of the fundamental image component (which manifests itself in *RMSE* oscillations) prevails over that due to wideband noise. Fig. 2 also shows that the BY1-LC and the Prony algorithms provide a little better overall accuracy than the c-IpDFTds one. Most probably this is due to the *ENBW* parameter of the Hann window employed in the proposed algorithm. The MP algorithm provides the most accurate amplitude and phase estimates. Specifically, when at least 3 cycles are analyzed, the worst *RMSE* values returned by the c-IpDFTds algorithm are only about 1.5 and 2-times higher than the best accuracies ensured by the Prony and the MP algorithms, respectively.

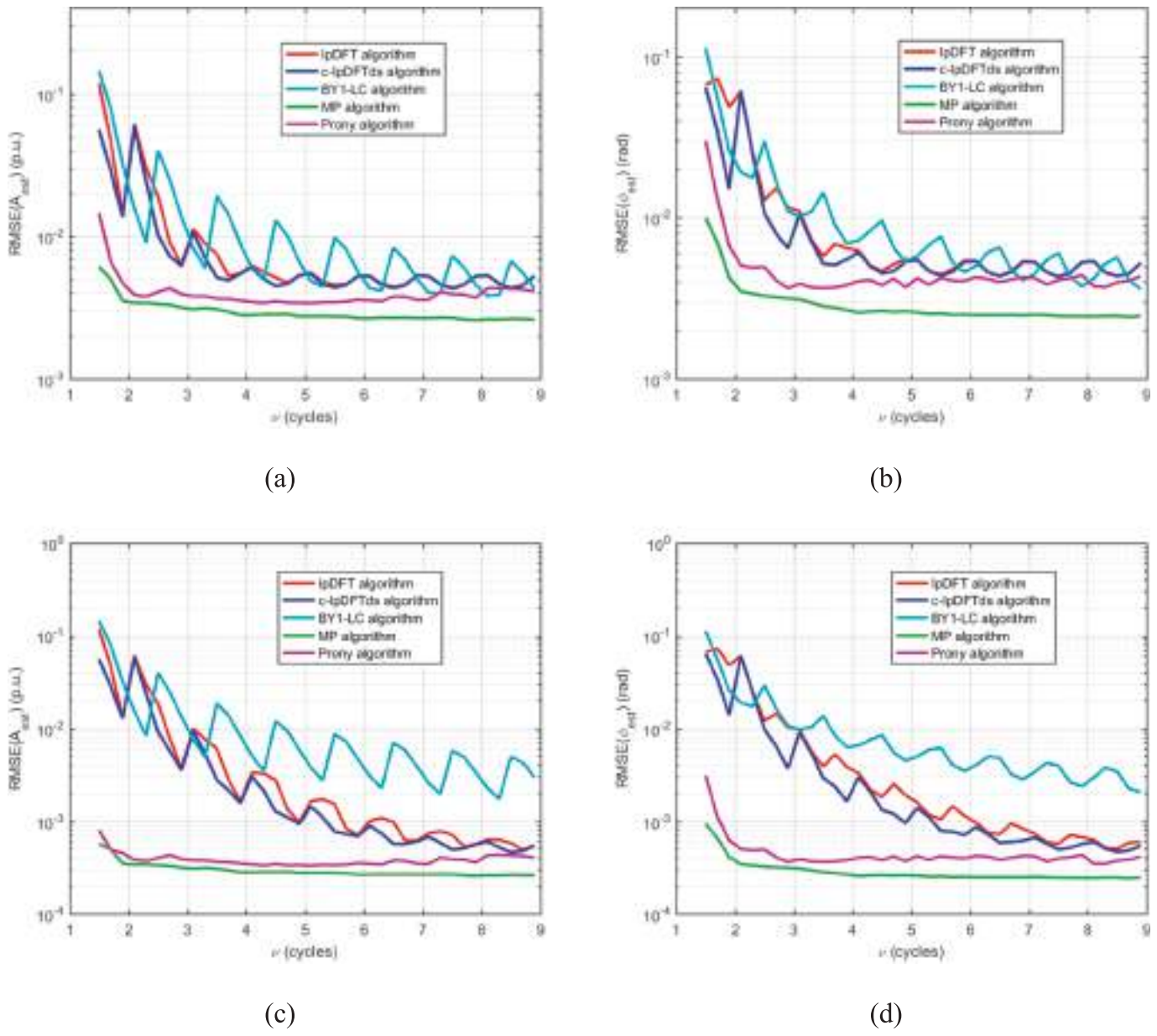

Fig. 5. Real-valued noisy and harmonically distorted damped sinusoids: *RMSE*s of the amplitude (a), (c) and phase (b), (d) estimates returned by the IpDFT, the c-IpDFTds, the BY1-LC, the MP, and the Prony algorithms versus the normalized frequency ν. $SNR = 40$ dB (a), (b) or $SNR = 60$ dB (c), (d), and $\alpha = 0.2$. Second and third damped harmonics with amplitudes 0.1 p.u. and 0.05 p.u., normalized decay rates 0.4 and 0.6, and phases selected at random. The two-term MSD ($H = 2$) window is adopted in the IpDFT and the c-IpDFTds algorithms. 10 iteratios are used in the BY1-LC algorithm, and the number of signal components is assumed known in the MP and the Prony algorithms. For each value of ν, 10,000 runs of $M = 128$ samples each are considered.

Fig. 3 shows the *RMSE*s of the signal amplitude (Fig. 3(a)) and phase (Fig. 3(b)) estimates returned by the considered algorithms as a function of the decay rate α which varies with a step of 0.05. $\nu = 2.3$ cycles and $SNR = 40$ dB or $SNR = 60$ dB.

As we can see, the *RMSE*s of both estimates returned by the considered algorithms increase with the decay rate. The accuracy of the classical IpDFT algorithm is the worst one and it is almost independent of *SNR* since it is mainly due to the contribution of the fundamental image component. When $SNR = 40$ dB, the c-IpDFTds, the BY1-LC, and the Prony algorithms have very close accuracies while, for $SNR = 60$ dB the difference between amplitude estimation *RMSE*s increases with α. The MP algorithm always ensures the best accuracy.

Fig. 4 shows the *RMSE*s of the signal amplitude (Fig. 4(a)) and phase (Fig. 4(b)) estimates returned by the considered algorithms as a function of the *SNR* which varies with a step of 5 dB. $\nu = 2.3$ cycles and $\alpha = 0.2$. The root mean squares of the corresponding CRLBs (RCRLBs) [33] are also shown in Fig. 4 to provide a theoretical reference.

At high *SNR* values, the accuracy of the classical IpDFT algorithm is clearly dominated by the contribution of the fundamental image component. The c-IpDFTds amplitude estimates show a residual effect of the image component when the *SNR* is higher than about 55 dB. However, it overcomes the Prony algorithm when wideband noise dominates (that is when the *SNR* is lower than about 20 dB), while the Prony algorithm provides better accuracy when the *SNR* is higher than about 50 dB. The BY1-LC algorithm provides accurate amplitude estimates for all considered *SNR* values. They are almost equally accurate as those returned by the c-IpDFTds algorithm when the *SNR* is smaller than about 55 dB, and more accurate for higher values of *SNR*s. As for the phase estimates, the c-IpDFTds, the BY1-LC, and the Prony algorithms are almost equally accurate in the whole range of considered *SNR* values.

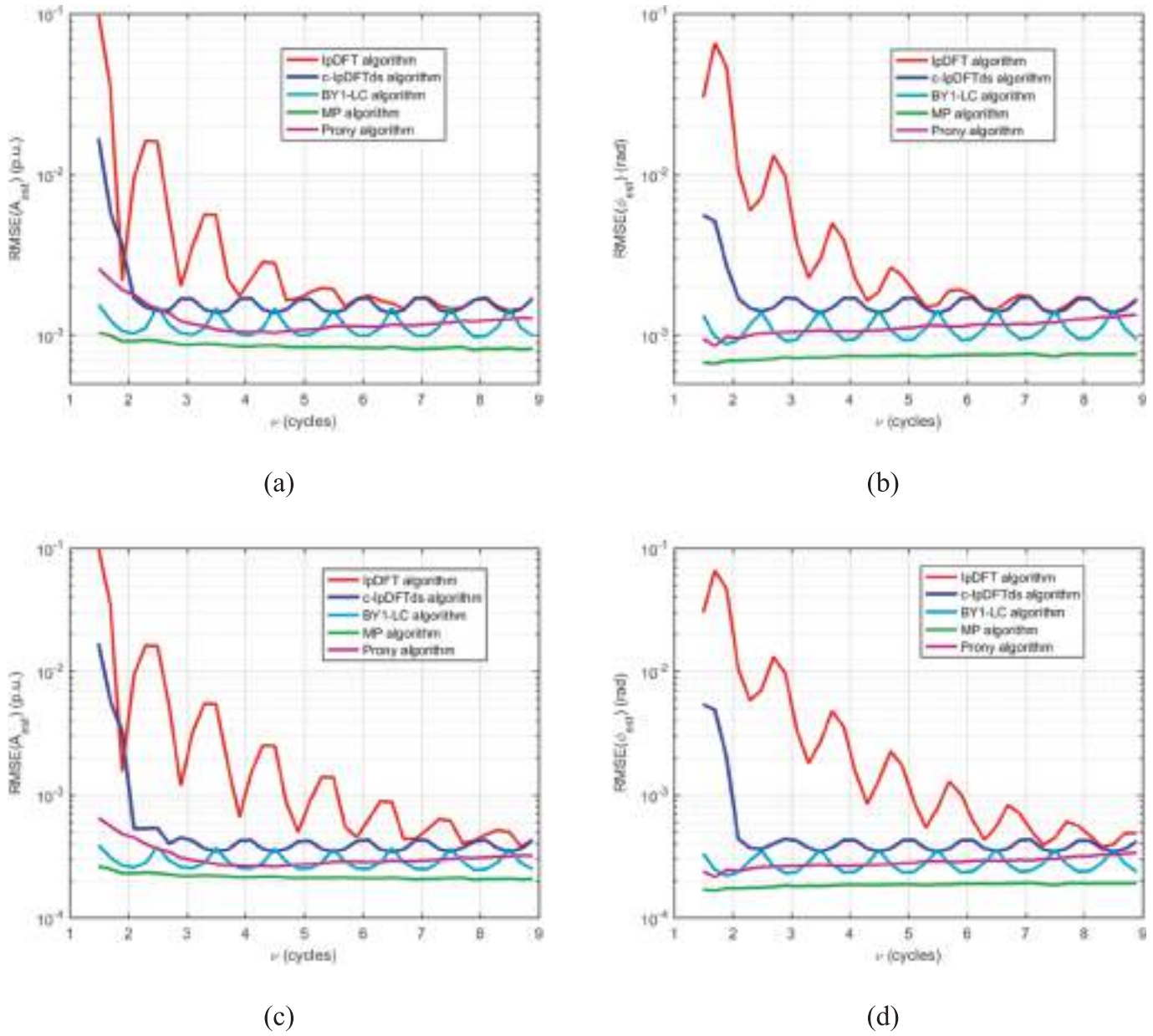

Fig. 6. Real-valued noisy damped sinusoids: *RMSE*s of the amplitude (a), (c) and the phase (b), (d) estimates returned by the IpDFT, the c-IpDFTds, the BY1-LC, the MP, and the Prony algorithms versus the normalized frequency ν when the signals are affected by 8 bit (a), (b) or 10 bit (c), (d) quantization noise; $\alpha = 0.2$. The two-term MSD ($H = 2$) window is adopted in the IpDFT and the c-IpDFTds algorithms. 10 iteratios are used in the BY1-LC algorithm, and the number of signal components is assumed known in the MP and the Prony algorithms. For each value of ν, 10,000 runs of $M = 128$ samples are considered.

The MP algorithm ensures the best accuracy, which is very close to the related RCRLB, as expected [16].

Real-valued noisy and harmonically distorted damped sinusoids are also generated by adding second and third damped harmonics to the signal analyzed above. The harmonic amplitudes and normalized decay rates are equal to 0.1 p.u. and 0.05 p.u., 0.4 and 0.6, respectively, while the related phases are randomly changed in the range $[0, 2\pi)$ rad. Fig. 5 shows the *RMSE*s of the amplitude and the phase estimates returned by the considered algorithms for the harmonically distorted damped sinusoids as a function of the normalized frequency ν when $SNR = 40$ dB (Fig. 5(a) and (b)) or $SNR = 60$ dB (Fig. 5(c) and (d)). Since the signal contains three tones, the model order of the MP algorithm is chosen equal to $K = 6$. Conversely, extensive simulations showed that the Prony algorithm provides accurate estimates when the model order $P = 2\left\lfloor \frac{M}{2l+1} \right\rfloor$ is selected, where the operator $\lfloor \bullet \rfloor$ returns the greatest integer smaller than its argument.

When few signal cycles are observed, so that the detrimental contribution of the fundamental image component dominates the one due to harmonics, the proposed c-IpDFTds algorithm may provide a smaller *RMSE*s than the classical one. Conversely, similarly to Fig. 2, the two IpDFT algorithms are almost equally accurate when at least about 4 cycles are observed if $SNR = 40$ dB or when at least about 7 cycles are analyzed if $SNR = 60$ dB. Thanks also to the additional information about the number of signal components, both the Prony and the MP algorithms ensure more accurate parameter estimates. Indeed, the knowledge of the model order allows the compensation of the effect of all the disturbance components. The BY1-LC algorithm exhibits the poorest performance in most situations. Indeed, the contribution of the spectral interference from harmonics to the estimated parameters is significant due to the adoption of the rectangular window.

The considered algorithm accuracies are also analyzed considering

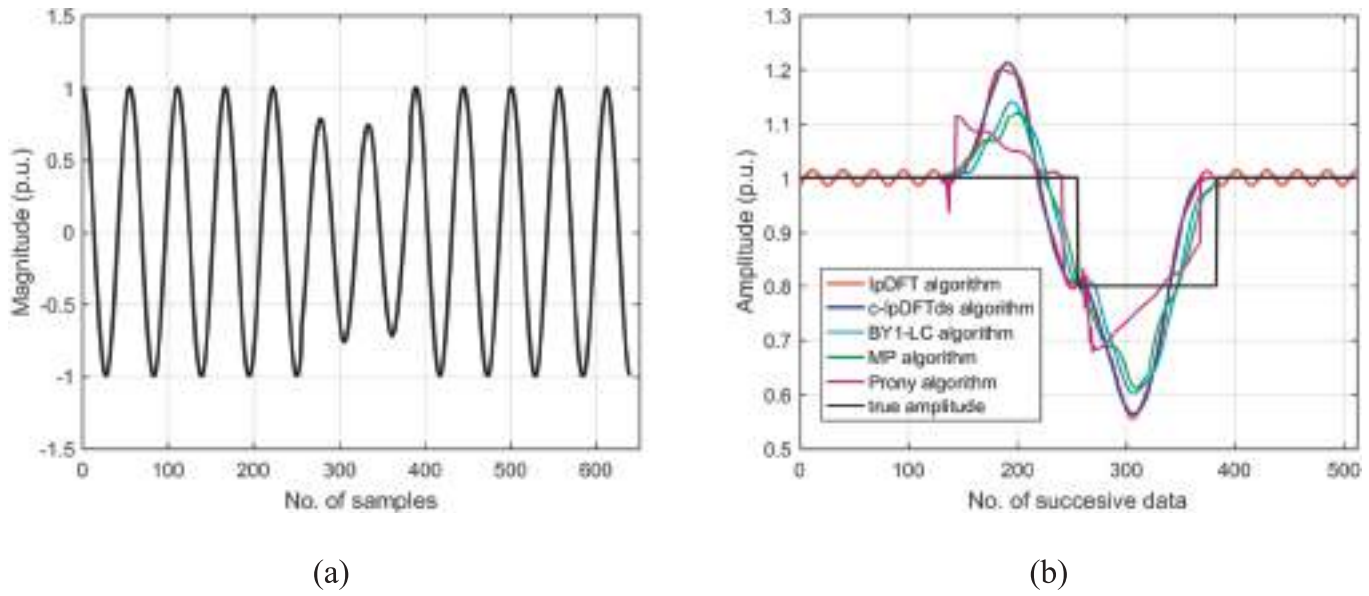

Fig. 7. Real-valued noisy undamped sinusoid affected by a transient modeled as damped sinusoid: (a) analyzed signal and (b) amplitude estimates returned by the IpDFT, the c-IpDFTds, the BY1-LC, the MP, and the Prony algorithms at each new acquired sample. Acquisition length of $M = 128$ samples. Sinusoid amplitude 1 p.u., damped sinusoid amplitude 0.8 p.u., and decay rate 0.02. Constant signal frequency equal to $\nu/M = 2.3/128$. The two-term MSD ($H = 2$) window is adopted in the IpDFT and the c-IpDFTds algorithms. 10 iteratios are used in the BY1-LC algorithm, and the number of signal components is assumed known in the MP and the Prony algorithms.

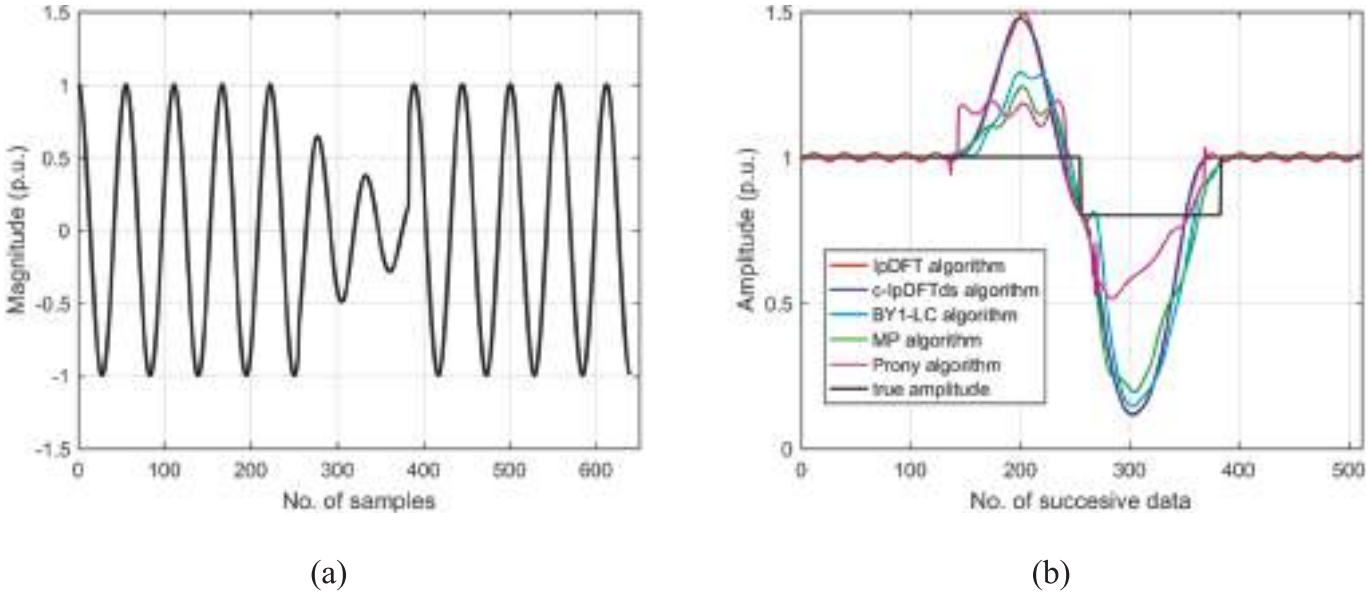

Fig. 8. Real-valued noisy undamped sinusoid affected by a transient modeled as damped sinusoid: (a) analyzed signal and (b) amplitude estimates returned by the IpDFT, the c-IpDFTds, the BY1-LC, the MP, and the Prony algorithms at each new acquired sample. Acquisition length of $M = 128$ samples. Sinusoid amplitude 1 p.u., damped sinusoid amplitude 0.8 p.u., and decay rate 0.2. Constant signal frequency equal to $\nu/M = 2.3/128$. The two-term MSD ($H = 2$) window is adopted in the IpDFT and the c-IpDFTds algorithms. 10 iteratios are used in the BY1-LC algorithm, and the number of signal components is assumed known in the MP and the Prony algorithms.

the effect of quantization modelled as white additive noise uniformly distributed. Fig. 6 shows the *RMSE*s of the obtained signal amplitude and phase estimates as a function of the normalized frequency ν, which varies with a step of 0.2 cycles. The effect of 8 bits (Fig. 6(a), (b)) and 10 bits (Fig. 6(c), (d)) quantization is considered and the normalized decay rate is $\alpha = 0.2$.

By comparing Figs. 6 and 2 it follows that, when the signal is affected by quantization noise, the behaviors of the algorithm accuracies are essentially the same as in the case of Gaussian noise, as already noticed in the literature for undamped sinusoids [34].

The behaviors of the considered algorithms when the damped sinusoid is due to a fault in a generator of sinusoidal signals is also analyzed. The analyzed signal is composed by three segments: a sinusoid of amplitude 1 p.u., phase $\pi/6$ rad, and duration 256 samples; a damped sinusoid of amplitude 0.8 p.u., decay rate 0.02 or 0.2, phase $3\pi/4$ rad, that lasts 128 samples; a sinusoid of amplitude 1 p.u., phase $\pi/3$ rad, with duration 256 samples. The observation window duration is $M = 128$ samples and the signal frequency is assumed constant in the whole record, that is $\nu/M = 2.3/128$ cycles/samples. The *SNR* is 60 dB and the signal amplitude estimates are updated with each new acquired sample.

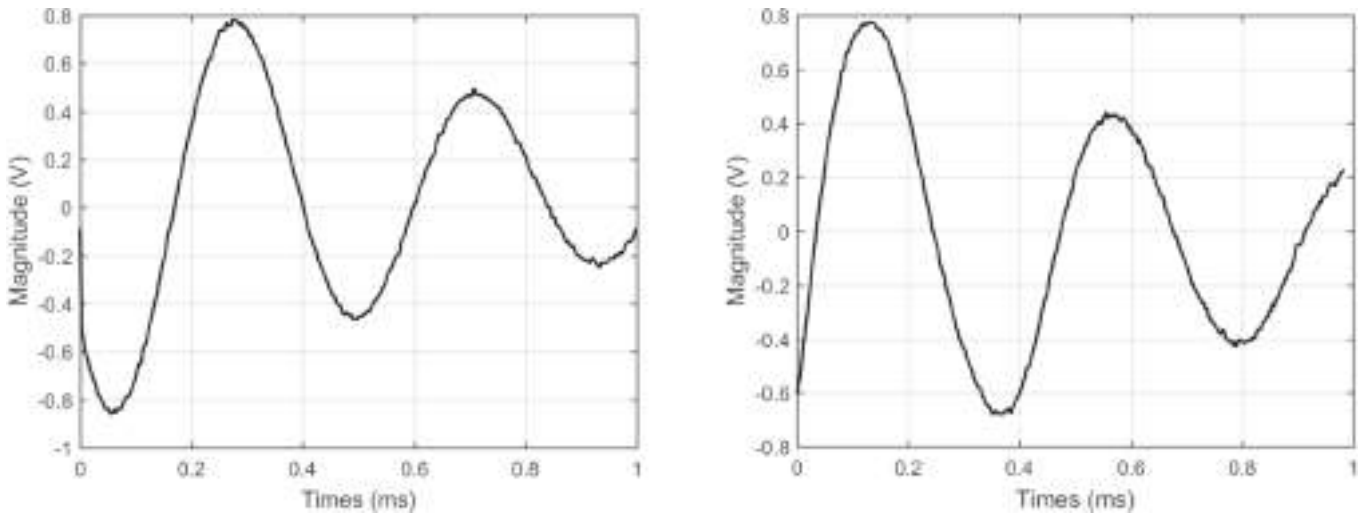

Fig. 9. A record of the acquired real-valued noisy damped sinusoid (a) and noisy and harmonically disrtorted damped siunusoid (b) versus the time. $\nu = 2.3$ cycles.

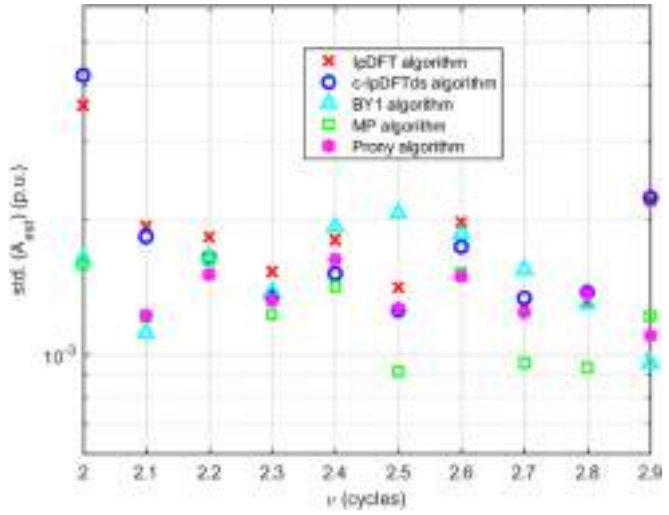

Fig. 10. Real-valued noisy damped sinusoids: experimental standard deviations of the amplitude estimates returned by the IpDFT, the c-IpDFTds, the BY1-LC, the MP, and the Prony algorithms versus the normalized frequency ν. SNR = 40 dB and $\alpha = 0.2$. The two-term MSD ($H = 2$) window is adopted in the IpDFT and the c-IpDFTds algorithms. 10 iteratios are used in the BY1-LC algorithm. Prony model order $P = 2\lfloor M/(2l+1)\rfloor$; MP model order K selected as proposed in [15] using threshold $3{\cdot}10^{-2}$. For each value of ν, 50 runs of $M = 391$ samples each are considered.

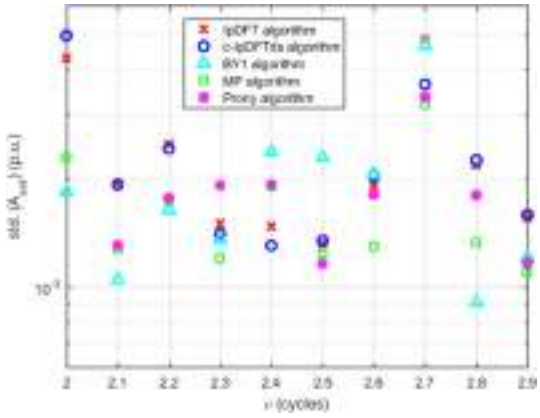

Fig. 11. Real-valued noisy and harmonically distorted damped sinusoids: experimental standard deviations of the amplitude estimates returned by the IpDFT, the c-IpDFTds, the BY1-LC, the MP, and the Prony algorithms versus the normalized frequency ν. SNR = 40 dB and $\alpha = 0.2$. Second and third damped harmonics with amplitudes 0.1 p.u. and 0.05 p.u., normalized decay rates 0.4 and 0.6, and phases selected at random. The two-term MSD ($H = 2$) window is adopted in the IpDFT and the c-IpDFTds algorithms. 10 iteratios are used in the BY1-LC algorithm. Prony model order $P = 2\lfloor M/(2l+1)\rfloor$; MP model order K selected as proposed in [15] using threshold $3{\cdot}10^{-2}$. For each value of ν, 50 runs of $M = 391$ samples each are considered.

The analyzed signals and the obtained amplitude estimates are shown in Figs. 7 and 8 when $\alpha = 0.02$ and 0.2, respectively.

Figs. 7 and 8 show that the c-IpDFTds, the BY1-LC, the MP, and the Prony algorithms provide very accurate steady state amplitude estimates, while the IpDFT estimates are affected by the interference from the fundamental image component. Conversely, when the analyzed record contains fault samples, all estimated amplitudes exhibit large variations regardless the value of the decay rate. Thus, all the considered algorithms can be effectively employed in the detection of faults, but they are not suitable for estimating the amplitude of the related transient.

5.2. Experimental results

In the experiments, real-valued noisy or noisy and harmonically distorted sinusoid samples are generated in MATLAB and saved in.csv data files. Data are then used to generate 1 kHz signals by using the arbitrary waveform generator of an USB oscilloscope PicoScope 2205A. After that, records of $M = 391$ samples are acquired with a sampling rate of 390.6 kSa/s in 1 ms window duration.

As in the simulations, the fundamental amplitude and the normalized decay rate are set to $A = 1$ V and $\alpha = 0.2$, respectively. The second and the third damped harmonics amplitudes and normalized decay rates are 0.1 V, 0.05 V, 0.4 and 0.6, respectively. The normalized frequency ν varies in the range [2.0, 2.9] with a step of 0.1 cycles. For each value of ν, 50 data records are acquired with phases at random. The SNR is set to 40 dB with respect to the fundamental. However, the acquired signals

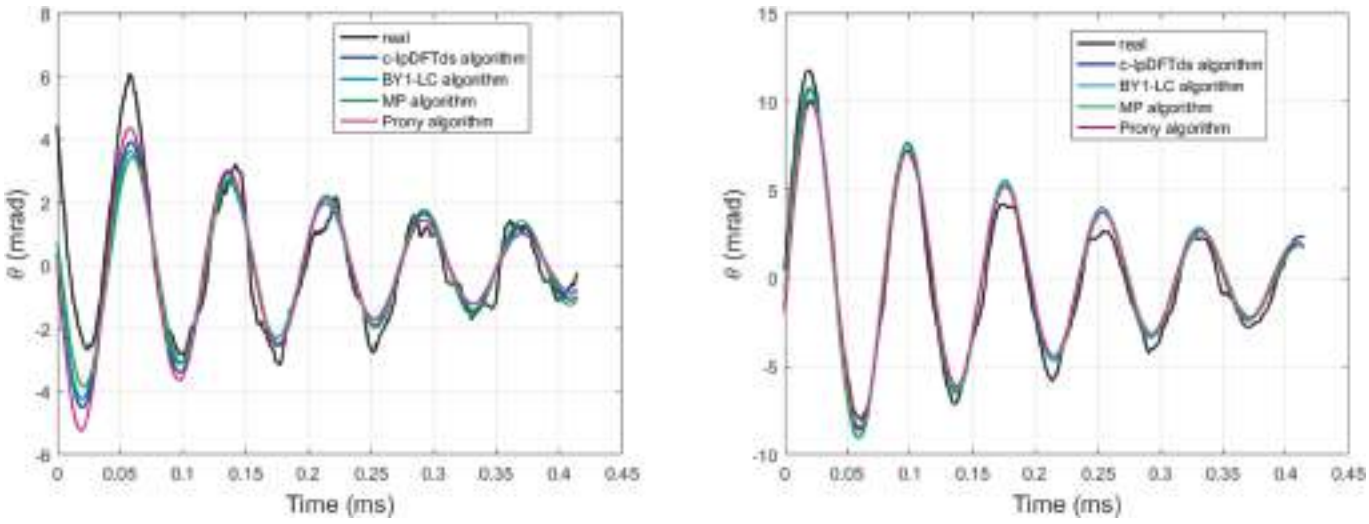

Fig. 12. Experimental results obtained by means of an optically pumped Cs magnetometer: real and estimated signals extracted from the transmitted (a) and the reflected (b) channels of the PBS. The synthesized signals are obtained using the parameters estimated by the c-IpDFTds, the BY1-LC, the MP, and the Prony algorithms. The two-term MSD ($H = 2$) window is adopted in the IpDFT and the c-IpDFTds algorithms. 10 iteratios are used in the BY1-LC algorithm. Prony model order $P = 2\lfloor M/(2l+1)\rfloor$; MP model order K selected as proposed in [15] using threshold $3{\cdot}10^{-2}$.

are also affected by the quantization noise of the oscilloscope 8-bit analog-to-digital converter, and the distortion introduced by the oscilloscope analog front-end.

A record containing $\nu = 2.3$ cycles of a noisy damped sinusoid or a noisy and harmonically distorted damped sinusoid are shown in Fig. 9 as a function of time.

Only the signal amplitude accuracy is investigated in the following since the signal phase takes random values in each record. The model order of the Prony algorithm is set to $P = 2\left\lfloor \frac{M}{2l+1} \right\rfloor$. As for the MP algorithm the procedure proposed in [15] and selecting heuristically a threshold of $3{\cdot}10^{-2}$.

Figs. 10 and 11 show the standard deviations of the amplitude estimates returned by the considered algorithms as a function of ν when the noisy damped sinusoids or the noisy and harmonically distorted damped sinusoids are analyzed, respectively. As expected, the obtained results agree with simulations performed with damped sinusoids affected by 8-bit quantization noise (Fig. 6(a)). Specifically, the MP algorithm provides the most accurate amplitude estimates in almost all considered situations, while the BY1-LC, the Prony, and the c-IpDFTds algorithms are almost equally accurate. Observe also that the standard deviations of experimental data exhibit the same ranges of variation as the *RMSE*s reported in Fig. 6(a). For harmonically distorted signals, the MP amplitude estimates generally exhibit a slightly better accuracy than the Prony method. Similarly to simulation results, the c-IpDFTds algorithm is a bit less performing than the Prony one and almost equally performing as the IpDFT algorithm. The BY1-LC algorithm provides accurate estimates only when ν is less than about 2.3 cycles or greater than about 2.8 cycles. For the other values of ν it exhibits a worse accuracy.

Experimental data obtained by means of an optically pumped Cs magnetometer [3] are also processed. The signals are extracted from the transmitted and the reflected channels of a polarizing beam splitter (PBS). Specifically, $M = 830$ signal samples are acquired by using a 12-bit digital oscilloscope with 2 MHz sampling rate [3]. Fig. 12 shows the actual signals and those synthesized using the parameters estimated by the c-IpDFTds, the BY1-LC, the MP, and the Prony algorithms. As in the previous experiment, the Prony model order is set to $P = 2\left\lfloor \frac{M}{2l+1} \right\rfloor$, while the optimal MP model order K is determined by applying the procedure proposed in [15] with threshold $3{\cdot}10^{-1}$ select heuristically.

Table 1
Estimated amplitudes, phases, and estimation error ε_Δ for the signals obtained from an optically pumped Cs magnetometer considering the transmitted and the reflected channels of a PBS.

Algorithm	FID – transmitted channel of the PBS			FID – reflected channel of the PBS		
	$\widehat{A}$(mrad)	$\widehat{\phi}$(rad)	ε_Δ (mrad)	$\widehat{A}$(mrad)	$\widehat{\phi}$(rad)	ε_Δ (mrad)
c-IpDFTds	4.86	1.49	0.94	11.04	4.56	0.83
BY1-LC	4.58	1.51	0.94	11.65	4.55	0.83
MP	4.10	1.39	0.89	11.81	4.64	0.79
Prony	5.72	1.59	1.04	11.78	4.50	0.87

Table 1 shows the estimated amplitudes $\widehat{A}$, phases $\widehat{\phi}$, and the *RMSE*s ε_Δ between the true and the estimated signals provided by the considered algorithms. As we can see, the *RMSE*s related to the signal of the reflected channel are smaller than those related to the transmitter channel data. On the whole, the MP amplitude estimates exhibit a slightly better accuracy than the c-IpDFTds algorithm, which is a bit more accurate than the Prony algorithm and has the same accuracy as the BY1-LC algorithm. The algorithm accuracies are confirmed in Fig. 12, which shows that the signal provided by the reflected channel is better tracked than the one of the transmitter channel, especially in the initial phase of the phenomenon.

6. Processing times comparison

As for the algorithm computational complexity, assuming that the number of analyzed samples M is a power of two, the IpDFT, the c-IpDFTds, and the BY1-LC algorithms require $O(M^2)$ or $O(M\log_2 M)$ complex additions and multiplications if the signal DFT is determined by using direct calculation or an FFT algorithm, respectively. The computational complexity of the Prony algorithm is of the order $O(P^3)$ due to the application of the least squares approach, while the application of the singular value decomposition used in the MP algorithm requires O(M^3) operations.

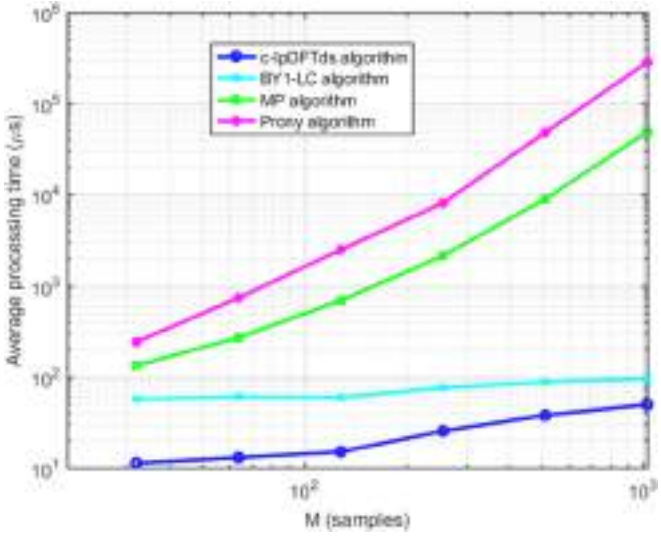

Fig. 13. Average processing times of the c-IpDFTds, the BY1-LC, MP, and Prony algorithms as a function of the number of analyzed samples.

The processing times required by the c-IpDFTds, the BY1-LC, the MP, and the Prony algorithms are determined as a function of the number of processed samples M using the MATLAB function *timeit*(·). The programs run on a laptop computer equipped with a Core i7-1165G7 at 2.80 GHz processor, 16 GB RAM, and Windows 10. A noisy damped sinusoid that exhibits $\nu = 3.3$ cycles and $SNR = 40$ dB is processed. The signal spectrum is determined by applying the function *fft*(·). The procedure proposed in [15] with threshold equal to $3{\cdot}10^{-2}$ is used to select the model order of the MP algorithm, while the Prony model order is equal to $P = 2\left\lfloor \frac{M}{2l+1} \right\rfloor$. Fig. 13 shows the average processing times required to process 200 runs of the analyzed algorithms.

As we can see, in the considered range for the number of analyzed samples, the processing time required by the c-IpDFTds algorithm is orders of magnitude smaller than those needed to implement the MP and the Prony algorithms and the computational advantage of the c-IpDFTds algorithm quickly increases with M. Moreover, the c-IpDFTds algorithm is computationally more efficient than the BY1-LC algorithm even if its relative efficiency decreases as M increases.

7. Conclusions

This paper dealt with the estimation of the amplitude and the phase of real-valued damped sinusoids by means of a frequency-domain approach. Analytical expressions for the contribution of the fundamental image component to the estimates returned by the classical IpDFT algorithm have been derived assuming that the acquired data are weighted by an MSD window. The derived expressions allowed an easy compensation of that detrimental effect, which enabled the proposal of the c-IpDFTds algorithm. The accuracy of the proposed algorithm is significantly better than the IpDFT algorithm one and close to those provided by the frequency-domain BY1-LC algorithm and the time-domain MP and Prony algorithms, widely used in the literature. Specifically, when at least about 1.5, but less than 3 sinusoid cycles are observed, the *RMSE* of the c-IpDFTds estimates is about 1.5 or 2 times the best *RMSEs* returned by the BY1-LC, the Prony or the MP estimates, respectively. Moreover, the c-IpDFTds algorithm outperforms the BY1-LC one and can provide even more accurate estimates than the MP or the Prony algorithms when the analyzed signals contain disturbing tones and the number of signal components is unknown, as often occurs in real-life situations. In addition, the processing time of the c-IpDFTds algorithm is orders of magnitudes smaller than the MP and the Prony algorithms and significantly smaller than the BY1-LC algorithm. For these reasons, the proposed c-IpDFTds algorithm can be advantageously employed when real-time accurate parameter estimates of noisy damped sinusoids are implemented in low-cost hardware platforms.

CRediT authorship contribution statement

Daniel Belega: Writing – original draft, Software, Investigation, Formal analysis, Conceptualization. **Dario Petri:** Writing – review & editing, Validation, Supervision, Methodology, Formal analysis.

Declaration of competing interest

The authors declare that they have no known competing financial interests or personal relationships that could have appeared to influence the work reported in this paper.

Acknowledgements

No Acknowledgements.

Appendix

Proof of Propositions 1 and 2

- Proof of Proposition 1

We can write:

$$\Psi(\alpha - \mathrm{j}\delta) = |\Psi(\alpha - \mathrm{j}\delta)|e^{\mathrm{j}\gamma_1}, \tag{A.1}$$

and

$$\Psi(\alpha + \mathrm{j}(2l+\delta)) = |\Psi(\alpha + \mathrm{j}(2l+\delta))|e^{\mathrm{j}\gamma_2}. \tag{A.2}$$

From (4) and (5) and (A.1) and (A.2) it follows that:

$$X_w(l) = A|\Psi(\alpha - \mathrm{j}\delta)| + A|\Psi(\alpha + \mathrm{j}(2l+\delta))|e^{-\mathrm{j}(\phi-\gamma_2)}, \tag{A.3}$$

From which:

$$|X_w(l)| \cong A|\Psi(\alpha - \mathrm{j}\delta)|\left|1 + \frac{|\Psi(\alpha + \mathrm{j}(2l+\delta))|}{|\Psi(\alpha - \mathrm{j}\delta)|}e^{-\mathrm{j}(2\phi+\gamma_1-\gamma_2)}\right|. \tag{A.4}$$

We have:

$$\left|1+\frac{|\Psi(\alpha+\mathrm{j}(2l+\delta))|}{|\Psi(\alpha-\mathrm{j}\delta)|}e^{-\mathrm{j}(2\phi+\gamma_1-\gamma_2)}\right| = \sqrt{1+\left(\frac{|\Psi(\alpha+\mathrm{j}(2l+\delta))|}{|\Psi(\alpha-\mathrm{j}\delta)|}\right)^2+2\frac{|\Psi(\alpha+\mathrm{j}(2l+\delta))|}{|\Psi(\alpha-\mathrm{j}\delta)|}\cos(2\phi+\gamma_1-\gamma_2)}$$

$$\cong 1+\frac{|\Psi(\alpha+\mathrm{j}(2l+\delta))|}{|\Psi(\alpha-\mathrm{j}\delta)|}\cos(2\phi+\gamma_1-\gamma_2), \tag{A.5}$$

where it is assumed that $\frac{|\Psi(\alpha+\mathrm{j}(2l+\delta))|}{|\Psi(\alpha-\mathrm{j}\delta)|}\ll 1$ and the formula $\sqrt{1+x}\cong 1+\frac{x}{2}$, for $|x|\ll 1$, is used.

By replacing (A.5) into (A.4) it follows that:

$$|X_w(l)|\cong A|\Psi(\alpha-\mathrm{j}\delta)|\left[1+\frac{|\Psi(\alpha+\mathrm{j}(2l+\delta))|}{|\Psi(\alpha-\mathrm{j}\delta)|}\cos(2\phi+\gamma_1-\gamma_2)\right]. \tag{A.6}$$

From (9) and (A.6) we have:

$$\widehat{A}=\left|\frac{X_w(l)}{\Psi(\widehat{\alpha}-\mathrm{j}\widehat{\delta})}\right|\cong A\frac{|\Psi(\alpha-\mathrm{j}\delta)|}{|\Psi(\widehat{\alpha}-\mathrm{j}\widehat{\delta})|}\left[1+\frac{|\Psi(\alpha+\mathrm{j}(2l+\delta))|}{|\Psi(\alpha-\mathrm{j}\delta)|}\cos(2\phi+\gamma_1-\gamma_2)\right]. \tag{A.7}$$

From (A.7), expression (11) can be easily obtained.

- Proof of Proposition 2

We have:

$$\Psi(\widehat{\alpha}-\mathrm{j}\widehat{\delta})=|\Psi(\widehat{\alpha}-\mathrm{j}\widehat{\delta})|e^{\mathrm{j}\widehat{\gamma}_1}. \tag{A.8}$$

Using (4), (A.1) and (A.8) it follows that:

$$\frac{X_w(l)}{\Psi(\widehat{\alpha}-\mathrm{j}\widehat{\delta})}=A\frac{|\Psi(\alpha-\mathrm{j}\delta)|}{|\Psi(\widehat{\alpha}-\mathrm{j}\widehat{\delta})|}e^{\mathrm{j}(\phi+\gamma_1-\widehat{\gamma}_1)}+A\frac{|\Psi(\alpha+\mathrm{j}(2l+\delta))|}{|\Psi(\widehat{\alpha}-\mathrm{j}\widehat{\delta})|}e^{-\mathrm{j}(\phi-\gamma_2+\widehat{\gamma}_1)}. \tag{A.9}$$

From (A.9), after simple algebra, it results that:

$$arg\left\{\frac{X_w(l)}{\Psi(\widehat{\alpha}-\mathrm{j}\widehat{\delta})}\right\}=\tan^{-1}\{\tan(\phi+\gamma_1-\widehat{\gamma}_1)\frac{1-\frac{|\Psi(\alpha+\mathrm{j}(2l+\delta))|}{|\Psi(\widehat{\alpha}-\mathrm{j}\widehat{\delta})|}\bullet\frac{\sin(\phi-\gamma_2+\widehat{\gamma}_1)}{\sin(\phi+\gamma_1-\widehat{\gamma}_1)}}{1+\frac{|\Psi(\alpha+\mathrm{j}(2l+\delta))|}{|\Psi(\widehat{\alpha}-\mathrm{j}\widehat{\delta})|}\bullet\frac{\cos(\phi-\gamma_2+\widehat{\gamma}_1)}{\cos(\phi+\gamma_1-\widehat{\gamma}_1)}}\right\}. \tag{A.10}$$

Since $(1+x)^{-1}\cong 1-x$, when $|x|\ll 1$, and neglecting the term containing the squared ratio of $\frac{|\Psi(\alpha+\mathrm{j}(2l+\delta))|}{|\Psi(\widehat{\alpha}-\mathrm{j}\widehat{\delta})|}$, after some calculations, it follows that:

$$arg\left\{\frac{X_w(l)}{\Psi(\widehat{\alpha}-\mathrm{j}\widehat{\delta})}\right\}\cong\tan^{-1}\{\tan(\phi+\gamma_1-\widehat{\gamma}_1)-\frac{|\Psi(\alpha+\mathrm{j}(2l+\delta))|}{|\Psi(\widehat{\alpha}-\mathrm{j}\widehat{\delta})|}\bullet\frac{\sin(2\phi+\gamma_1-\gamma_2)}{\cos^2(\phi+\gamma_1-\widehat{\gamma}_1)}\}. \tag{A.11}$$

Expressing the $\tan^{-1}(\bullet)$ function using the Taylor's series about $\tan(\phi+\gamma_1-\widehat{\gamma}_1)$, and truncating the expansion to the first order term, since $\frac{|\Psi(\alpha+\mathrm{j}(2l+\delta))|}{|\Psi(\widehat{\alpha}-\mathrm{j}\widehat{\delta})|}\bullet\left|\frac{\sin(2\phi+\gamma_1-\gamma_2)}{\cos^2(\phi+\gamma_1-\widehat{\gamma}_1)}\right|\ll 1$, after some calculations (A.11) becomes:

$$\widehat{\phi}=arg\left\{\frac{X_w(l)}{\Psi(\widehat{\alpha}-\mathrm{j}\widehat{\delta})}\right\}\cong\phi+\gamma_1-\widehat{\gamma}_1-\frac{|\Psi(\alpha+\mathrm{j}(2l+\delta))|}{|\Psi(\widehat{\alpha}-\mathrm{j}\widehat{\delta})|}\bullet\sin(2\phi+\gamma_1-\gamma_2). \tag{A.12}$$

From (A.12) expression (12) can be easily obtained.

Data availability

No data was used for the research described in the article.

References

[1] H. Günther, NMR Spectroscopy: Basic Principles, Concepts and Applications in Chemistry, John Wiley & Sons, 2013.

[2] Z.D. Grujić, P.A. Koss, G. Bison, A. Weis, A sensitive and accurate atomic magnetometer based on free spin precession, Eur. Phys. J. D 69 (135) (2015).

[3] D. Hunter, S. Piccolomo, J.D. Pritchard, N.L. Brockie, T.E. Dyer, E. Riis, Free-induction-decay magnetometer based on a microfabricated Cs vapor cell, Phys. Rev. Appl. 10 (2018).

[4] D. Hunter, R. Jiménez-Martínez, J. Herbsommer, S. Ramaswamy, W. Li, E. Riis, Waveform reconstruction with a Cs based free-induction-decay magnetometer, Opt. Express 26 (23) (2018) 30523–30531.

[5] S. Fricke, J. Seymour, M. Battistel, D. Freedberg, C. Eads, M. Augustine, Data processing in NMR relaxometry using the matrix pencil, J. Magn. Reson. 313 (2020).

[6] J.C. Visschers, O. Tretiak, D. Budker, L. Bougas, Continuous-wave cavity ring-down polarimetry, J. Chem. Phys. 152 (2020).

[7] L. Bougas, D. Sofikitis, G.E. Katsoprinakis, A.K. Spiliotis, P. Tzallas, B. Loppinet, T. P. Rakitzis, Chiral cavity ring-down polarimetry: chirality and magnetometry measurements using signal reversals, J. Chem. Phys. 143 (2015).

[8] Estimation of Electromechanical Modes in Power Systems using Synchronized Phasor Measurements and Applications for Control of Inter-Area Oscillations, A contribution to CIGRE WG B5-14 Wide Area Protection and Control Technologies (2013).

[9] J.A. de la O Serna, Synchrophasor estimation using Prony's method, IEEE Trans. Instrum. Meas. 62 (8) (2013) 2119–2128.

[10] A. Fort, E. Landi, R. Moretti, P. Carbone, A. Moschitta, Damped sine wave parameter extraction: application to QCM-D signals for accurate measurements, IEEE Trans. Instrum. Meas. 74 (2025).

[11] K. Duda, T.P. Zielinski, Efficacy of the frequency and damping estimation of a real-value sinusoid, IEEE Instrum. Meas. Mag. 16 (2) (2013) 48–58.

[12] S.L. Marple, Digital Spectral Analysis, Prentice-Hall, Englewood Cliffs, NJ, 1987.

[13] C.-I. Chen, G.W. Chang, An efficient Prony-based solution procedure for tracking of power system voltage variations, IEEE Ind. Electron. 60 (7) (2013) 2681–2688.

[14] Y. Hua, T.K. Sarkar, Matrix pencil method for estimating parameters of exponentially damped/undamped sinusoid in noise, IEEE Trans. Acoust. Speech Signal Process. 38 (5) (1990) 814–824.

[15] T.K. Sarkar, O. Pereira, Using the matrix pencil method to estimate the parameters of a sum of complex exponentials, IEEE Trans. Antennas Propag. Mag. 37 (1) (1995) 48–55.
[16] Y. Hua, T.K. Sarkar, Generalized pencil-of-function method for extracting poles of an EM system from its transient response, IEEE Trans. Antennas Propag. 37 (2) (1989).
[17] C. Offelli, D. Petri, Interpolation techniques for real-time multifrequency analysis, IEEE Trans. Instrum. Meas. 39 (1) (1990) 106–111.
[18] E. Aboutanios, Estimation of the frequency and decay factor of a decaying exponential in noise, IEEE Trans. Signal Process. 58 (2) (2010) 501–509.
[19] E. Aboutanios, Estimating the parameters of sinusoids and decaying sinusoids in noise, IEEE Instrum. Meas. Mag. 14 (2) (2011) 8–14.
[20] M. Bertocco, C. Offeli, D. Petri, Analysis of damped sinusoidal signals via a frequency-domain interpolation algorithm,, IEEE Trans. Instrum. Meas. 43 (2) (1994) 245–250.
[21] R. Diao, Q. Meng, An interpolation algorithm for discrete Fourier transforms of weighted damped sinusoidal signals, IEEE Trans. Instrum. Meas. 63 (6) (2014) 1505–1523.
[22] R. Diao, Q. Meng, H. Fan, Interpolation algorithms based on Rife-Vincent window for discrete Fourier transforms of damped signals, J. Mech. Eng. 51 (2015) (in Chinese).
[23] D. Belega, D. Petri, Frequency and damping factor estimation of real-valued damped sinusoids by means of an improved two-point interpolated DFT algorithm, Digital Signal Process. 153 (2024).
[24] J. Song, A. Mingotti, J. Zhang, L. Perotto, H. Wen, Accurate damping factor and frequency estimation for damped real-valued sinusoidal signals, IEEE Trans. Instrum. Meas. 71 (2022).
[25] R.C. Wu, C.T. Chiang, Analysis of the exponential signal by the interpolated DFT algorithm, IEEE Trans. Instrum. Meas. 59 (12) (2010) 3306–3317.
[26] D. Belega, D. Petri, D. Dallet, Generalized multi-point interpolated DTFT frequency and damping factor estimators of real-valued damped sinusoids, Meas 234 (2024).
[27] K. Duda, T.P. Zielinski, L.B. Magalas, M. Majewski, DFT based estimation of damped oscillation's parameters in low frequency mechanical spectroscopy, IEEE Trans. Instrum. Meas. 60 (11) (2011) 3608–3618.
[28] H. Xu, S. Zhou, B. Yan, Parameter estimation for a damped real-valued sinusoid in noise, Rev. Sci. Instrum. 92 (2021).
[29] K. Wang, H. Wen, W. Tai, G. Li, Estimation of damping factor and signal frequency for damped sinusoidal signal by three points interpolated DFT, IEEE Signal Process Lett. 26 (12) (2019) 1927–1930.
[30] H. Wu, L. Fan, X. Zhao, M. Li, L. Lu, J. Jin, Frequency and damping factor estimation of damped sinusoid by using DFT and DTFT, Measurement 242 (2025).
[31] A.H. Nuttall, Some windows with very good sidelobe behavior, IEEE Trans. Acoust. Speech Signal Process. (1981) 84–91. ASSP-29(1).
[32] D. Belega, D. Dallet, Multifrequency signal analysis by interpolated DFT method with maximum sidelobe decay windows, Measurement 42 (3) (2009) 420–426.
[33] Y. Yao, S.M. Pandit, Cramér-Rao lower bounds for a damped sinusoidal process, IEEE Trans. Signal Process. 43 (4) (1995) 878–885.
[34] C. Offelli, D. Petri, The influence of windowing on the accuracy of multifrequency signal parameter estimation, IEEE Trans. Instrum. Meas. 41 (2) (1992) 256–261.